Tale of two planets p. 475 ▸

Global versus local water p. 478

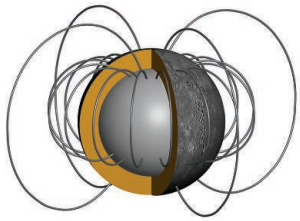

PERSPECTIVES

ROBOTICS

Two leaps forward for robot locomotion

Biomimetic robots can jump on land and on water

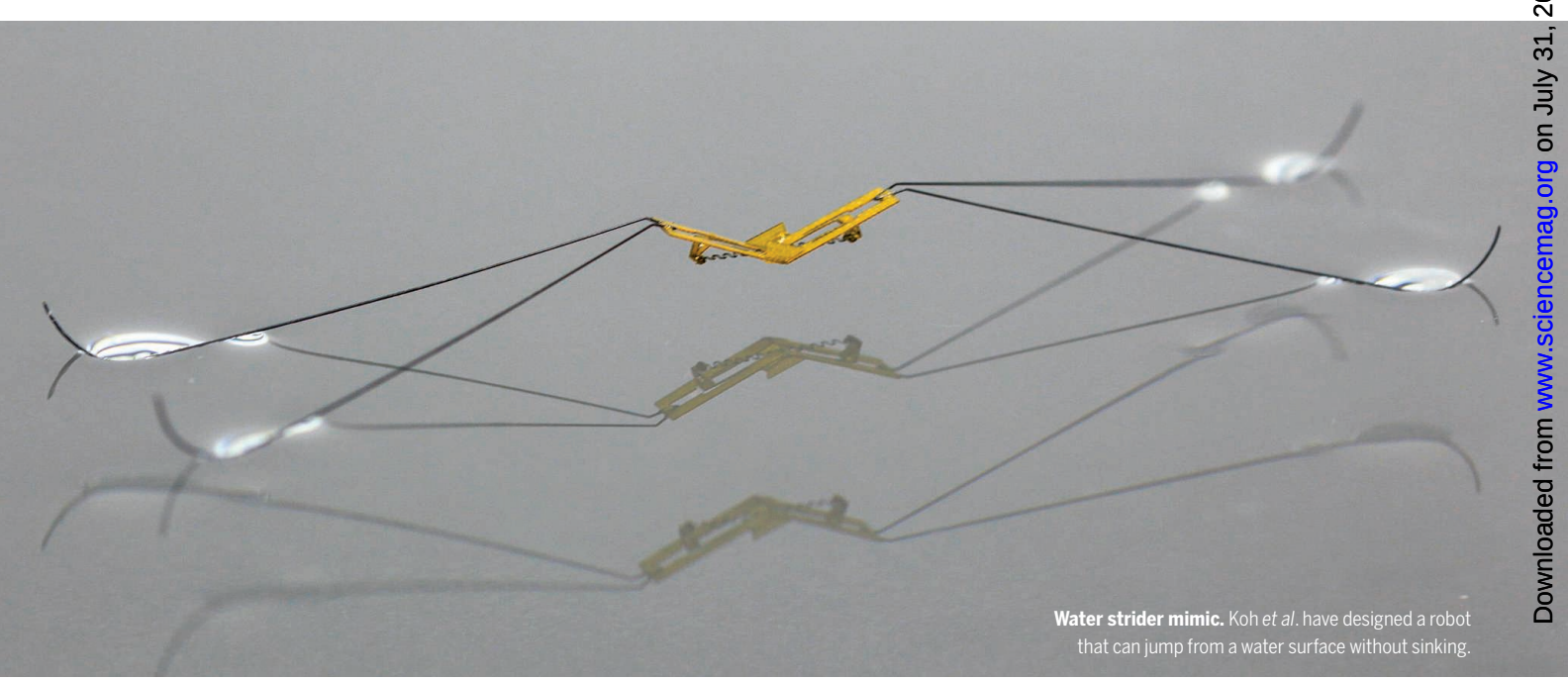

Water strider mimic. Koh *et al*. have designed a robot that can jump from a water surface without sinking.

By **Dominic Vella**

The designers of mobile robots often take their inspiration from animals. In recent years, examples have included SmartBird, a flying robot that is modeled on a herring gull; BigDog, a rough-terrain robot that can walk, run, climb, and carry heavy loads; and the humanoid Asimo. With the exception of SmartBird, however, these robots can only move horizontally and over land. Being able to cope with different terrains remains a key challenge for robotics. Perhaps no two terrains are more different than land and water, and yet several animals can move equally well on either (*1*). On page 517 of this issue, Koh *et al*. describe a robot that is so at home on the water surface that it can leap to heights of 14 cm without piercing the surface (*2*).

Walking and jumping on water poses a number of challenges for robots that motion on land does not. Most obviously, the robot must stay afloat, which in general means that it must be sufficiently small—dense objects smaller than a few centimeters can float thanks to the surface tension of water (*3*). However, producing small, water-walking robots requires ingenious engineering. The first water-walking robot, RoboStrider (*4*), was intended as a proof-of-principle for the "rowing" mechanism employed by water striders. Its design was extremely simple, with a twisted rubber band storing the energy to drive its legs. Subsequent refinements of RoboStrider (*5*) and other water-walking robots (*6*) have used more sophisticated actuation mechanisms, but the motion has remained almost exclusively horizontal.

However, the most remarkable feature of water-walking insects is their agility and, in particular, their ability to jump clear of the water surface. Replicating these jumps has proved to be a severe technical challenge: Jumping requires the robot to push down on the water surface, potentially endangering its precarious state at the surface and ultimately causing it to sink.

To design a robot capable of jumping from water, Koh *et al*. first studied carefully how real water striders jump. This revealed that rather than pushing purely downwards, they rotate their legs, accelerating the motion rap-

Mathematical Institute, Andrew Wiles Building, Woodstock Road, Oxford OX2 6GG, UK.
E-mail: dominic.vella@maths.ox.ac.uk

PHOTO: BIOROBOTICS LAB/SEOUL NATIONAL UNIVERSITY

idly and allowing the insects to attain high vertical accelerations without piercing the water surface. It also allows the insects to jump as high on water as they can on land, distinguishing this mechanism from that used by other semi-aquatic insects that can jump much more effectively on dry land (*7*).

Revealing the mechanics of water strider jumping was only the first step; Koh *et al.* took further inspiration from flea jumps and used "pop-up" manufacturing to create a simple, light mechanism that can generate the rapid sweeping motion needed. The result is strikingly similar to the jumping of the real water strider. What is more, the robot jumps on water equally well as, and sometimes better than, on land.

To generate the rapid sweeping motion of the legs, Koh *et al.* use the snap-through of a hinge. However, this motion is triggered by an external heat source, rather than by the robot itself. A completely different solution to this rapid actuation problem has been suggested recently (albeit on dry land). Bartlett *et al.* (*8*) reported a soft robot that uses the controlled explosion of an oxygen-butane mixture to generate the large accelerations needed to jump. The high energy density of the oxygen-butane mixture makes this a promising way to generate up to 30 jumps without refueling. However, the extreme forces involved mean that thought needs to be given to the materials used in construction: Soft parts are important to allow jumping, but a partly rigid top focuses the acceleration downward and enhances the jumping efficiency. Using computer simulations and experiments, Bartlett *et al.* showed that the ideal combination is to grade the material from soft to hard. This grading also makes the robot more robust and can now be achieved relatively easily with multimaterial three-dimensional printing.

For many soft robots, the necessity of making a rapid leap will be a relatively rare occurrence, rather than the primary mode of locomotion. If so, instabilities of soft, elastic materials offer the ability to produce rapid motions and can be primed over much longer time scales. Examples of this abound in the plant kingdom, where several species use variants of the snap-through instability that is also seen in the popular hopper popper children's toy (*9*). For example, the Venus flytrap (*10*) and fern sporangium (*11*) both store elastic energy gradually but release it rapidly to generate extremely rapid motions. Taking inspiration from plants (rather than animals) to facilitate robot locomotion sounds counterintuitive, but it seems a possibility that has thus far been underexploited. ■

High jump expert. Koh *et al.* based their design on a detailed study of water strider motion. For movies of robot and water strider motion, see the supplementary materials in (*2*).

PHOTO: DENNIS DRENNER/VISUALS UNLIMITED/CORBIS

REFERENCES

1. J. W. M. Bush, D. L. Hu, *Annu. Rev. Fluid Mech.* **38**, 339 (2006).
2. J.-S. Koh *et al.*, *Science* **349**, 517 (2015).
3. D. Vella, *Annu. Rev. Fluid Mech.* **47**, 115 (2015).
4. D. L. Hu, B. Chan, J. W. M. Bush, *Nature* **424**, 663 (2003).
5. D. L. Hu, M. Prakash, B. Chan, J. W. M. Bush, *Exp. Fluids* **43**, 769 (2007).
6. O. Ozcan, H. Wang, J. D. Taylor, M. Sitti, *Int. J. Adv. Robot. Syst.* **11**, 85 (2014).
7. M. Burrows, G. P. Sutton, *Curr. Biol.* **22**, R990 (2012).
8. N. W. Bartlett *et al.*, *Science* **349**, 161 (2015).
9. A. Pandey, D. E. Moulton, D. Vella, D. P. Holmes, *Europhys. Lett.* **105**, 24001 (2014).
10. Y. Forterre, J. M. Skotheim, J. Dumais, L. Mahadevan, *Nature* **433**, 421 (2005).
11. X. Noblin *et al.*, *Science* **335**, 1322 (2012).

10.1126/science.aac7882

ORGANIC CATALYSIS

A leap ahead for activating C-H bonds

Boron-based catalysts add functional groups to normally unreactive carbon-hydrogen bonds

By **Shubhankar Kumar Bose** *and* **Todd B. Marder**

Although great strides have been taken in recent decades, the catalytic and selective functionalization of normally unreactive carbon-hydrogen bonds (*1*) as a route to high value-added compounds remains one of the major challenges in catalysis, and in chemistry in general. On page 513 of this issue, Légaré *et al.* (*2*) describe a metal-free process for the catalytic borylation of carbon-hydrogen bonds in heteroarenes. Their catalyst incorporates a "frustrated" pair comprising a Lewis acid and base, and this approach to the problem may have wider applications in other carbon-hydrogen bond functionalization reactions.

As synthetic intermediates, organoboronate esters and boronic acids (*3*) feature in the synthesis of pharmaceuticals, agrochemicals, liquid crystals, and organic light-emitting diodes. Their importance is, in part, the result of the Suzuki-Miyaura cross-coupling reaction (*4*) but also because of their applications in other carbon-carbon, carbon-oxygen, carbon-nitrogen, and carbon-halogen bond-forming processes and the ease with which the boronate moiety can be replaced by a wide variety of functional groups. Boronates are not only among the most useful intermediates in contemporary organic synthesis but also appear directly in new boron-containing drugs—for example, the anticancer agent bortezomib (Velcade) and antifungal agent tavaborole (Kerydin). Boronates are being explored as biologically relevant sensors for sugars and hydrogen peroxide, as building blocks for novel covalent organic framework materials for gas storage, and in hydrogels, among other applications.

Thus, it is not surprising that interest in new methods for their synthesis has increased enormously. Boronates are often air- and water-stable reagents, tolerant to many

Two leaps forward for robot locomotion

Dominic Vella

Science **349**, 472 (2015);
DOI: 10.1126/science.aac7882

BIOMECHANICS

Jumping on water: Surface tension–dominated jumping of water striders and robotic insects

Je-Sung Koh,[1,2]* Eunjin Yang,[3]* Gwang-Pil Jung,[1] Sun-Pill Jung,[1] Jae Hak Son,[4] Sang-Im Lee,[4,5] Piotr G. Jablonski,[4,6] Robert J. Wood,[2] Ho-Young Kim,[3,5]† Kyu-Jin Cho[1,5]†

Jumping on water is a unique locomotion mode found in semi-aquatic arthropods, such as water striders. To reproduce this feat in a surface tension–dominant jumping robot, we elucidated the hydrodynamics involved and applied them to develop a bio-inspired impulsive mechanism that maximizes momentum transfer to water. We found that water striders rotate the curved tips of their legs inward at a relatively low descending velocity with a force just below that required to break the water surface (144 millinewtons/meter). We built a 68-milligram at-scale jumping robotic insect and verified that it jumps on water with maximum momentum transfer. The results suggest an understanding of the hydrodynamic phenomena used by semi-aquatic arthropods during water jumping and prescribe a method for reproducing these capabilities in artificial systems.

Water striders skate easily on the surface of water mainly because their low body mass and superhydrophobic legs allow them to be supported on their tarsi (the proximal segment of an arthropod's foot) by surface tension alone (*1*–*3*). They are able to generate sufficient vertical propulsion to disengage or jump from the water surface—actions that require high momentum with a high vertical take-off velocity.

Previous studies of the mechanics of water-"walking" in a variety of animals, from small insects to reptiles, elucidated the mode of momentum transfer to the water (*1*–*6*): The velocity of the driving leg was found to play a dominant role. Comparatively heavy animals with a high Baudoin number [$Ba = Mg/(\sigma P) >> 1$, where M is the mass, g is the gravitational acceleration, $\sigma = 72$ mN m^{-1} is the surface tension of water at 25°C, and P is the contact perimeter] cannot float on the surface, so they commonly use high driving power and speed to generate inertial forces in the water large enough to support their weight. For example, the basilisk lizard paddles its foot downward to expand an air cavity under the water and then pulls its foot out of the water before the cavity collapses (*7*). Limb strokes at velocities higher than 30 ms^{-1} induce large hydrodynamic forces, including viscous drag and inertia from the water. In contrast, small arthropods covered with water-repellent integuments (a skin of the arthropod) can float on water without effort because of surface tension ($Ba < 1$). Hu *et al.* (*1*, *4*), Denny (*5*, *8*), and Suter *et al.* (*3*) have reported plausible propulsion mechanisms for small water surface–dwelling animals. These animals achieve horizontal momentum transfer by generating a capillary wave on the water surface and vortices beneath the surface.

Although several small-scale robots inspired by the water strider have demonstrated the ability to float and locomote on water by partly or fully using surface tension (*4*, *9*, *10*), none of them jumps on water. Furthermore, jumping that involves interactions between the unconstrained free body and the liquid surface has been poorly understood at the scale of insects (*11*, *12*). Jumping is vertical propulsion, and it requires different criteria from walking on water, which is lateral propulsion. In contrast to jumping on solid ground, a large driving force and fast stroke in the jumping leg do not guarantee a high take-off velocity on the water surface, especially for small insects (*11*, *12*). There are small insects, such as pygmy mole crickets, that still manage to jump on water by taking advantage of viscosity via a high driving acceleration and leg velocity (>130,000° s^{-1}). But their water-jumping performance is much lower than when they jump on solid ground (*13*).

Water striders can jump on water as high as they can jump on land (*1*). When they are exposed to danger, they show extremely high jumping performance and land in an uncontrolled manner. We focused on this extreme case that achieves the maximum momentum transfer on water. To explore this amazing semi-aquatic motility, we collected water striders (*Aquarius paludum*) from a local pond and recorded them jumping on water in the laboratory with high-speed cameras (Fig. 1A and materials and methods section 1). We found that their ability to exploit the water surface comes from maximizing momentum transfer to the body, which is the integration of force with respect to time by Newton's second law of motion. That is, the water strider gradually increases its leg force to the limit allowed by the water surface and maintains that force until it disengages from the water surface.

High-speed imaging experiments revealed that the insect rises upward while pushing the water surface downward and closing four of its legs inward (Fig. 1A). The hydrodynamic forces generated during this leg motion include drag, surface tension, buoyancy, inertia, and viscous friction. On the basis of estimates of each force using representative values of parameters for the insects we observed (tables S4 and S5), we found that the surface tension force dominates the other forces (supplementary text section 2) for the Weber number, $We = \rho U^2 D/\sigma \sim 10^{-2}$, and $Ba = Mg/(\sigma P) \sim 10^{-2}$. Here, ρ is the density of water, $U \sim 0.2$ m s^{-1} is the rate of dimple growth (i.e., the depression resulting from the force imparted by the leg), $D \sim 0.1$ mm is the leg diameter, $M \sim 40$ mg is the mass of the insect, and $P \sim 80$ mm is the perimeter of the legs that defines the contact length. The low value for We, because of the slow stroke with a thin leg, implies a small energy loss through water flow compared with the interfacial energy of the curved water surface. This inertia-free interaction between the legs and the water surface ensures that the legs remain in contact with the water surface during the down stroke, thereby fully exploiting the reaction force of the curved meniscus on the legs. If the legs struck the water at high speed, the water surface would retreat fast enough to lose contact with the legs and splashing would ensue, decreasing the efficiency of momentum transfer between the legs and water surface (*12*). The combination of a light body with a long perimeter (low Ba) indicates an ability to generate an extremely high body acceleration (compared with g) by using the surface tension of water. Consequently, low We and Ba collectively contribute to the high acceleration of a jumping body through surface tension–dominant interaction without notable energy loss to the water.

A small We, implying negligibly small dynamic effect on the interaction between the legs and the meniscus (*14*), allows the use of static calculations of interfacial force based on the depth of the meniscus (see supplementary text section 2 and table S1). Because the surface tension force on a floating wire tends to increase with the depth of the dimple (figs. S10 to S12) (*15*), it is desirable to push the water surface as deeply as possible. However, the meniscus ruptures when the leg descends beyond the depth limit that the surface tension of water can endure, leading to a dramatic reduction of the reaction force on the

[1]Biorobotics Laboratory, Department of Mechanical and Aerospace Engineering, Seoul National University, Seoul 151-744, Korea. [2]School of Engineering and Applied Sciences and Wyss Institute for Biologically Inspired Engineering, Harvard University, Cambridge, MA 02138, USA. [3]Micro Fluid Mechanics Laboratory, Department of Mechanical and Aerospace Engineering, Seoul National University, Seoul 151-744, Korea. [4]Laboratory of Behavioral Ecology and Evolution, School of Biological Sciences, Seoul National University, Seoul 151-742, Korea. [5]Institute of Advanced Machines and Design, Seoul National University, Seoul 151-744, Korea. [6]Museum and Institute of Zoology, Polish Academy of Sciences, Warsaw 00-679, Poland.
*These authors contributed equally to this work.
†Corresponding author. E-mail: hyk@snu.ac.kr (H.-Y.K.); kjcho@snu.ac.kr (K.-J.C.)

jumping body (*16*). A superhydrophobic straight cylinder of negligible diameter lying horizontally on a water surface can depress the interface roughly by the capillary length (*17*) without sinking. The load supported by a floating object is equal to the weight of water displaced by the body and the perturbed free surface (*18*). It has already been suggested that adaptive deformation of joints and the flexibility of the tibia and tarsus of the water strider's leg may prevent the tip of the leg from piercing the water meniscus and increase the supporting force of the water surface by increasing the water volume displaced (*19*). Figure 1B shows that the tapered leg keeps its tip pointing upward during the stroke, helping to prevent rupture of the meniscus. By using a theoretical model to deduce the force acting on a flexible cylinder floating on liquid (with two parallel contact lines along its axis), we found that the maximum force per unit length (f) on the legs of the water striders is always close to but below a value corresponding to twice the surface tension of water, 144 mN m^{-1}, which is the maximum value that water surface can withstand (Fig. 1C, supplementary text section 2, and table S1).

Careful observation of the jumping sequence of the water strider (Fig. 1A) reveals that the insect rotates its middle and hind legs rather than merely pushing them downward. That is, legs that are initially sprawled on the water surface are extended downward at take-off through actuated leg rotation. To explain the mechanical advantages of this leg movement, we consider what would happen if the leg morphology and kinematics were such that the water strider could depress the surface only vertically without rotation. Upon reaching the maximum dimple depth, l_c, the meniscus is recovered at a velocity of $U \sim l_c/t_r \sim 10^{-1}$ m s^{-1}, where t_r is the time scale for the capillary-gravity wave to travel the capillary length (*20*, *21*). This is far lower than the take-off velocity of the real water strider, $V \sim 1$ m s^{-1}, as evidenced by the relatively slower recovery of the meniscus (from 0 to 14 ms in Fig. 1A) compared with fast disengagement of the legs from the water surface. This implies that the fast-rising water strider would be able to use the upward force from the meniscus only while the legs contact and depress the water surface, thereby significantly reducing the time for momentum transfer. In reality, however, the water strider rotates its legs during jumping, which ensures that the legs meet an undistorted water surface continuously. Thus, the legs can keep pressing the water surface to the maximum depth during ascent of the body despite the slow recovery speed of the meniscus. Our observation reveals that the extended time of interaction between the water surface and the rotating legs of the four water striders tested leads to an increase of V of 27% to 42% as compared with the case when the legs are assumed to move only vertically. Therefore, water striders maximize momentum transfer to the water surface by maintaining a high force profile on each leg until the last moment of jumping by depressing the water surface to the capillary length while rotating their legs.

On the basis of our understanding of real water striders, we identified design criteria for our at-scale robot. Superhydrophobic legs and a low body mass compared with surface tension, yielding Ba <<1, are conducive to higher acceleration with maximum use of surface tension force. In addition, to maximize the kinetic energy transfer to the robot instead of the water, locomotion with low descent velocity and thin legs (We « 1) are required. The driving force should be gradually increased to the maximum value of 144 mN m^{-1} (2σ) to prevent the robot's legs from penetrating the water surface during a jump. If the water surface is broken, the legs swing rapidly under the water surface, leading to high levels of splash and flow around the legs that dissipate energy, rendering jumping highly inefficient (Fig. 2). These criteria guarantee surface tension–dominant propulsion with minimal energy dissipation to water flow.

An ultralight impulsive system that can maximize momentum transfer with limited maximum driving force is required. Leg rotation is also required to ensure that the legs continuously meet an undistorted water surface and keep pressing the water surface. The leg shape should be designed to maximize the surface tension force in the same way as the flexible legs of water striders adapt to the dimple. Especially, the shape of the tip is strongly related to the wetted length when the legs of the water strider rotate inward (*17*). Therefore, the leg tip should be curved in order to

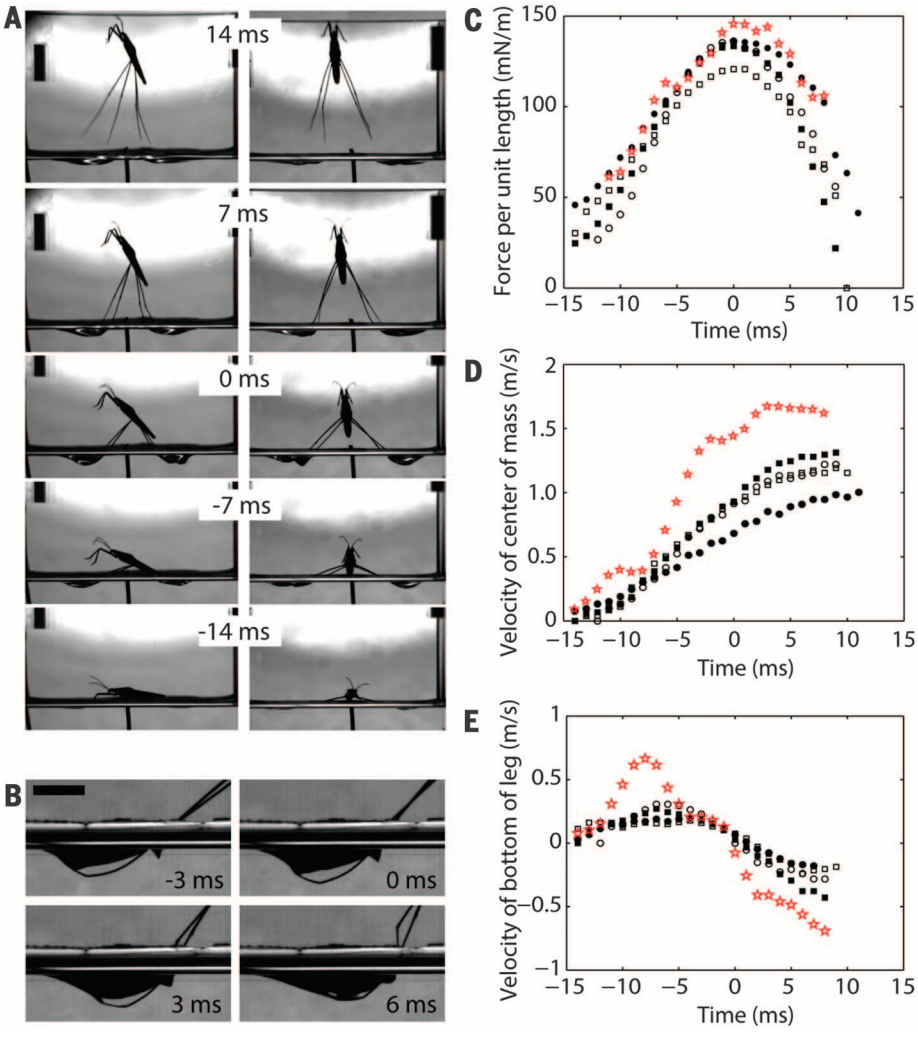

Fig. 1. Water strider jumping. (**A**) Jumping sequence of a water strider in side view (left column) and front view (right column). The black bars on the walls are 10-mm-long scale bars. See movie S5. (**B**) Bent leg of a water strider pushing the water surface. The wetted part of the leg moves to the right, resulting in meeting an undistorted water surface continuously. The scale bar indicates 5 mm. (**C**) f on the four legs of four water striders and robot 4. (**D**) Velocity profile of the water striders and robot 4 jumping from water. (**E**) Velocity profile of the bottom of the leg for water striders and robot 4. (C to E) Black symbols indicate four different water striders, and red stars indicate robot 4. The time is set to be zero when the maximum force is generated. See tables S1 and S3 for detail descriptions of the water striders and the robot.

adapt to the dimple with increasing wetted length while the legs rotate. The low *We* constraint can be rewritten as $t \gg (\rho h^2 D/\sigma)^{1/2}$ by using $U \sim h/t$, where h is the maximum dimple depth and t is the interaction time with water, which results in $t \gg 10^{-3}$ s for both real water striders and our at-scale robot (tables S1 to S4).

The robot uses a bio-inspired catapult mechanism adapted from a flea (*22*, *23*) and implemented with flexure hinge–based composite structures (*24*). The torque reversal catapult (TRC) mechanism in the flea's jumping leg is capable of rapid and repeatable torque production without complex mechanisms. It generates a very small torque when initially triggered, and the torque gradually increases through the driving stroke, as shown in Fig. 3G. This torque profile results in high momentum transfer from the water surface to the jumping body. In contrast, a high initial torque would create a large splash and waves on the water surface. Gradually increasing the torque minimizes unnecessary energy transfer to the water, allowing the jumping body to obtain maximum momentum.

The catapult mechanism uses composite materials and planar shape memory alloy (SMA) actuators. A similar TRC mechanism was previously developed to build a small-scale ground-jumping robot (*22*, *23*). The driving forces for our jumping robot can be varied by changing actuator stiffness and leg length. The passive trigger, which is the compliant beam component that holds the actuator, determines the required force for triggering the geometrical latch of the TRC and the stiffness of the actuator at the moment of triggering (fig. S6). This automatic triggering mechanism simplifies the latch system of the robot and makes it possible to minimize the size and weight of the structure. The 68-mg body weight is 6% of the maximum surface tension force that water can support (on legs with a 160-mm-long perimeter), corresponding to a *Ba* of 0.06, much less than 1 (table. S5). Theoretically, the robotic water strider can be vertically accelerated by a surface tension force up to 15 *g*. In jumping experiments, the robot achieved 13.8 *g*, which is close to the maximum acceleration.

When the legs swing, the length of the leg influences the reaction force on the legs primarily because it determines the moment arm of the driving legs, which transfers the torque generated by the TRC mechanism into a vertical reaction force. In nature, one long-legged water-jumping arthropod was shown to have driving legs 170% longer than its body (*16*). To reduce the maximum reaction force below the maximum surface tension force, we made the robot's legs 5 cm, longer than those of a water strider, because of the higher torque capabilities of the robot.

The pop-up book microelectromechanical system (MEMS) fabrication process (*24*–*28*) allowed us to build at-scale prototypes just 2 cm in body length and 68 mg in weight (Fig. 3D). This fabrication process avoids complex assembly steps by leveraging self-assembly techniques inspired by the folded components of pop-up books. This paradigm for fabricating micro- and "meso"-scale robots (*22*–*28*) is based on flexure hinge–based folded composites. The process involves layering and laminating sheets of individual materials, then folding the composite into a three-dimensional structure (fig. S5). The flexure hinges eliminate

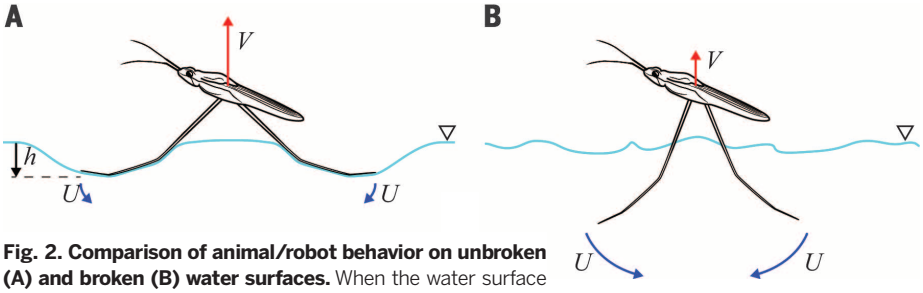

Fig. 2. Comparison of animal/robot behavior on unbroken (A) and broken (B) water surfaces. When the water surface is broken ($f > 2\sigma$), the force supporting the legs sharply reduces, causing the legs to swing rapidly into the water. The resulting viscous drag and splashing dissipate energy.

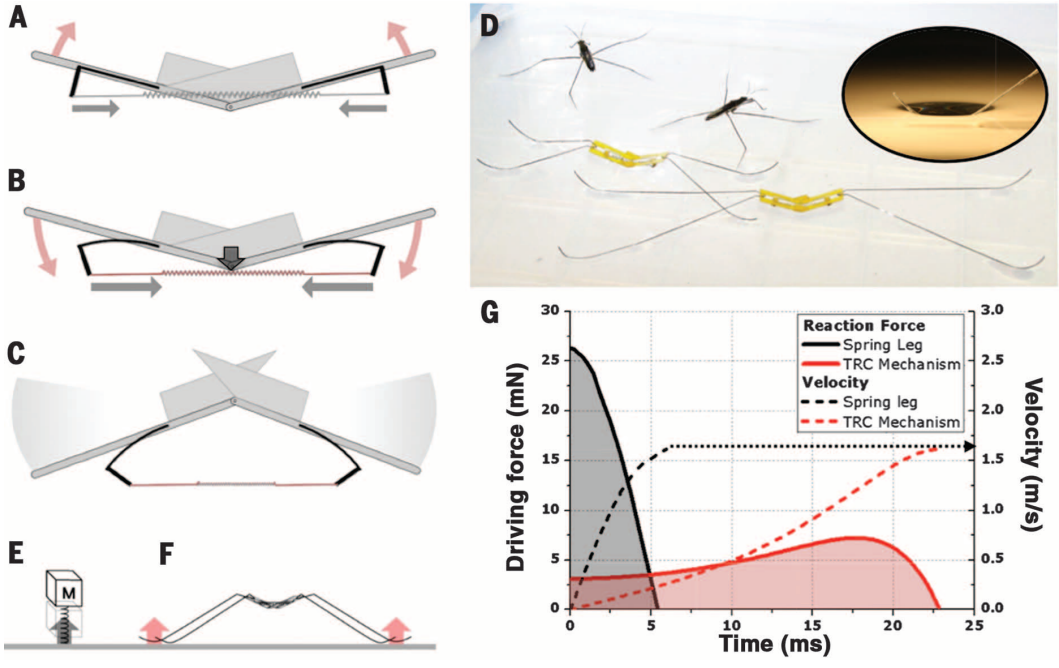

Fig. 3. The TRC mechanism inspired by a flea's jumping leg. (**A** to **C**) The principle of the mechanism. (A) Initial position. The actuator (shown as a coil) is attached at each compliant L-shaped cantilever. The actuator pulls the structure upward, but stoppers block the movement. (B) The actuator begins bending down the compliant L-shaped cantilever, which also moves the actuator down. (C) When the actuator passes through the center joint (i.e., the singularity of the mechanism), the torque direction is reversed, and the structure swings rapidly. The stored energy in the actuator and the cantilevers is released at once. (**D**) Two jumping robotic insects with different leg lengths, along with real water striders. The legs are coated with a hydrophobic material, resulting in a high contact angle that creates a dimple (inset image) on the water surface, which supports the weight of the robot. (**E** and **F**) Comparison of two jumping mechanisms, compressed spring legs (E) and a TRC mechanism (F). In contrast to the spring leg, a TRC mechanism may reduce the driving force on the legs by its torque characteristics and long length of the legs. (**G**) The driving force and velocity profiles of compressed spring legs and a TRC mechanism. The TRC mechanism requires much less maximum force to attain the same velocity. In comparison, the stroke of the actuators (springs) in both models is 5.75 mm, and their stiffness is set to generate the same *V* of 1.6 m s^{-1} (4.4 N m^{-1} in spring leg, 16.52 N m^{-1} in TRC mechanism).

friction, one of the dominant causes of energy loss and nonlinearity for small devices. The design parameters are determined by analyzing the compliance of the structure for passively triggering the torque reversal mechanism (see supplementary text section 1 and fig. S6) based on a fully dynamic simulation, including the mechanical properties of all the components and the interface forces between the water surface and the robot's legs (see supplementary text section 2 and fig. S13). Furthermore, all modeling steps are verified and supported by individual experiments. With this simple joint element, dynamic modeling and simulations match well with experimental data obtained with physical prototypes (fig. S3).

The sheet nickel titanium (NiTi) SMA actuator is embedded in the body structure as an artificial muscle. The sheet SMA was cut into a serpentine shape by the same ultraviolet laser micromachining system used to construct the body. The actuator is 80 μm thick, 100 μm wide, and 1 mg in weight. When heated above its transition temperature, the actuator's stiffness changes, inducing a negative strain and pulling the passive trigger in the body structure until the torque direction is reversed (Fig. 3, A to C).

The legs are made of superelastic Ni-Ti alloy to prevent them from permanent deformation during repeated jumping experiments. The high modulus and superelasticity of this wire permits the legs to be thin and flexible. The end tips of the wire legs in the robot (corresponding to the tarsus in the insect) are curved, which minimizes contact shape change between the legs and the water surface when the legs swing and prevents stress concentration at the interface between the tip and the water surface. The round shape of the wire leg linearizes the resulting surface tension force on the water surface as dimple depth increases, according to the experimental and theoretical modeling results shown in figs. S10 and S12. The linear surface tension force profile allowed us to model the hydrodynamic reaction force between the legs and the water as a spring (see supplementary text section 2 and table S6). This model yields simulations that are well matched with our experiments (within 7% error in V; see table S2).

The wire legs are coated with a superhydrophobic material, Everdry (Ultratech International Incorporated, Jacksonville, FL) (*29*). We achieved more than 150° of contact angle with this coating (supplementary text section 5 and fig. S9). Hydrophobicity increases jumping velocity by reducing downward forces when the legs escape from the free surface (*21*, *30*) and by increasing the maximum static load that water can endure (*6*, *20*, *21*, *30*, *31*). In particular, the superhydrophobic coating on the wire legs would lead to near zero adhesion to the water when they leave the surface (*21*).

We built five prototype robots that use different triggering forces. The driving force has a linear relationship with the triggering force. We performed jumping experiments with the prototypes on both water and ground (figs. S1 to S4 and table S2). A thin heating wire was carefully placed just below the robot body to activate the SMA actuator. As the SMA actuator transitions, the force increases, and the passive trigger begins to bend (Fig. 3, A to C). When the actuator passes through the center joint, the torque direction changes, and the body structure folds downward, generating a rapid snap-through.

The experiments verified the design criteria that the driving force per wetted length (f) should be below the maximum surface tension force per wetted length (2σ) in order for the robot to efficiently jump on water with maximum momentum transfer. Figure 4 shows that the robot jumps off the water surface smoothly without breaking the free surface and without making a large splash. V is 1.6 m s^{-1}, with a jumping height of 142 mm, and the maximum reaction force of the dimple is 9.27 mN. When the legs do not penetrate the water surface, the dynamic model

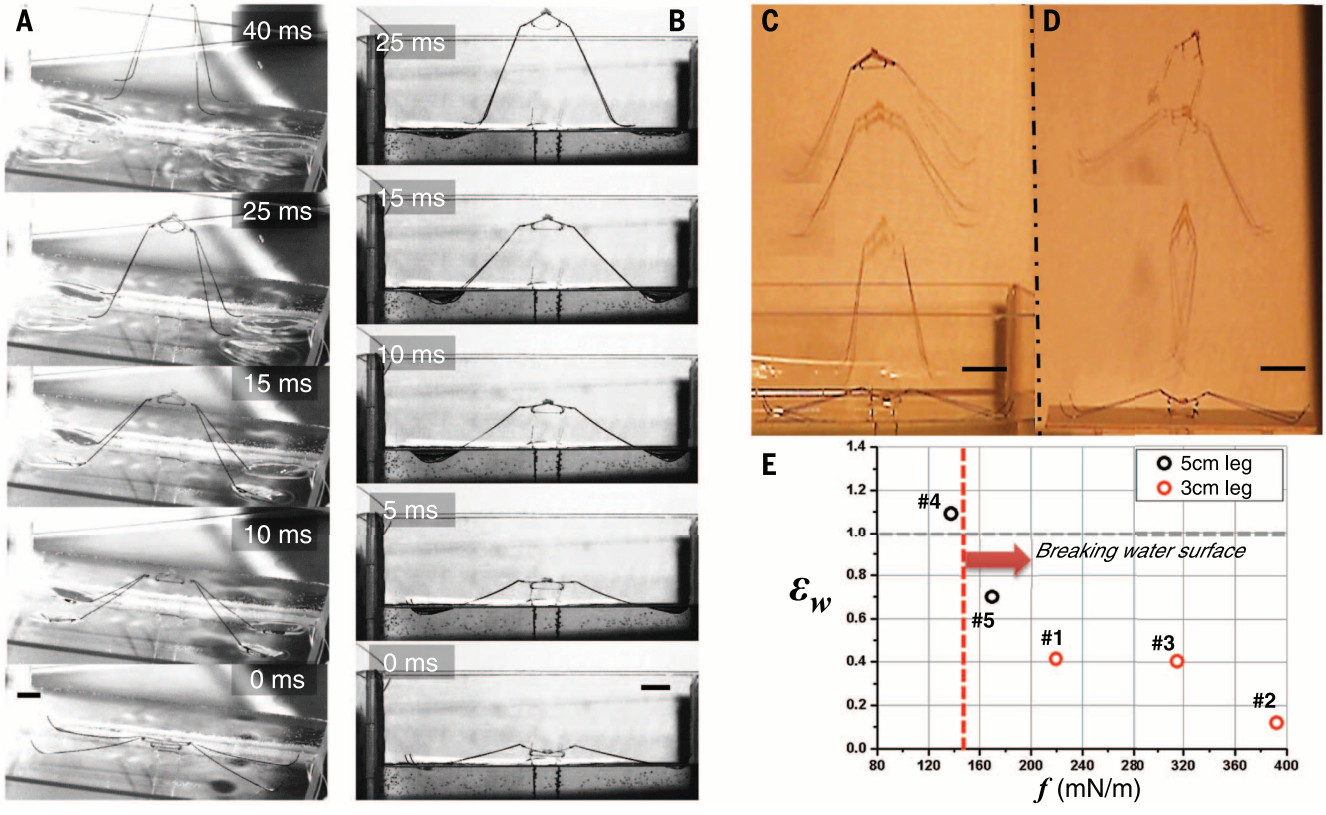

Fig. 4. Video frames of robot 4 and ε_w of robots jumping on water and on ground. (See movies S1 to S4.) (**A**) The legs distort the water surface. Note the absence of large splashing around the driving legs. (**B**) These horizontal views show that the legs do not penetrate the water surface. (**C**) Superimposed frames of the robot jumping on water. (**D**) Superimposed frames of the robot jumping on rigid ground. The robot obtains similar momentum on water and ground. Scale bar, 1 cm. (**E**) Experimental results for ε_w depending on different driving f of five robot prototypes. The red dashed line indicates the maximum surface tension force that water provides (2σ, 144 mN m^{-1}). The gray dashed line indicates a ε_w of 1.

of the robot jumping on water agrees well with experimental data, and we can obtain various reliable simulations from the model (supplementary text section 3 and fig. S3). The maximum driving f obtained from the dynamic model is 140 mN m^{-1}, just below the 144 mN m^{-1} (2σ) limit. Prototypes that satisfied the design criteria achieved higher take-off velocity on water (Fig. 4C) than when jumping on ground (Fig. 4D), a counterintuitive result. This may result from a reduction of leg vibration when jumping on water, because the stored energy is transferred into vertical kinetic energy rather than vibration energy. The movie of these jumps supports this proposition (movie S4). In our models, the initial energy stored in the actuator is 0.304 mJ and the jumping kinetic energy of the robot jumping on water is 0.095 mJ (31.3%), whereas the vibration kinetic energy is 0.193 mJ (63.5%) (table S7).

The water-ground velocity ratio (ε_w) describes how much momentum the robot attains on water compared with jumping on solid ground.

$$\text{Water} - \text{ground velocity ratio } (\varepsilon_w) = \frac{\text{Take} - \text{off velocity on water}}{\text{Take} - \text{off velocity on ground}}$$

A ratio lower than 1 indicates that the robot did not achieve as much momentum on water as on ground. If the driving force on water is kept below the maximum surface tension force defined by the design criteria, the ratio can be equal to or greater than 1, as was the case for robot 4, which had a maximum driving f just below the maximum surface tension force (2σ) (Fig. 4E). ε_w values of other prototypes are lower than 1, which means that the water surface is broken because of driving force that exceeds this limit, and thus the take-off velocity on water is reduced (table. S2 and fig. S3). High driving force does not guarantee a high take-off velocity in a surface tension–dominant case, as shown in robots 1 to 3 and 5. The maximum driving force is constrained by the surface tension coefficient of water. We may assume that water striders control their muscles precisely to satisfy these criteria in a manner similar to the design of the impulsive actuation mechanism in robot 4 (Fig. 1C).

Our at-scale water-jumping robotic insect has demonstrated that it is possible to reproduce the performance of water-jumping arthropods and has proved to be an effective tool for verifying theoretical insights on how the surface tension force can play a dominant role in locomotion of these systems. The experimental results improve our understanding of the dynamic interaction between an unconstrained free body and a liquid surface, as observed in semi-aquatic arthropods in nature.

REFERENCES AND NOTES

1. D. L. Hu, J. W. M. Bush, *J. Fluid Mech.* **644**, 5–33 (2010).
2. J. W. M. Bush, D. L. Hu, *Annu. Rev. Fluid Mech.* **38**, 339–369 (2006).
3. R. Suter, O. Rosenberg, S. Loeb, H. Long, *J. Exp. Biol.* **200**, 2523–2538 (1997).
4. D. L. Hu, B. Chan, J. W. M. Bush, *Nature* **424**, 663–666 (2003).
5. M. W. Denny, *Air and Water: The Biology and Physics of Life's Media* (Princeton Univ. Press, Princeton, NJ, 1993).
6. X. Gao, L. Jiang, *Nature* **432**, 36–36 (2004).
7. J. W. Glasheen, T. A. McMahon, *Nature* **380**, 340–342 (1996).
8. M. W. Denny, *J. Exp. Biol.* **207**, 1601–1606 (2004).
9. Y. S. Song, M. Sitti, *IEEE Trans. Robot.* **23**, 578–589 (2007).
10. X. Zhang *et al.*, *ACS Appl. Mater. Interfaces* **3**, 2630–2636 (2011).
11. D.-G. Lee, H.-Y. Kim, *Langmuir* **24**, 142–145 (2008).
12. B. Shin, H.-Y. Kim, K. J. Cho, Towards a biologically inspired small-scale water jumping robot. *2nd IEEE RAS and EMBS International Conference on Biomedical Robotics and Biomechatronics* (2008), pp. 127–131.
13. M. Burrows, G. P. Sutton, *Curr. Biol.* **22**, R990–R991 (2012).
14. D. Vella, J. Li, *Phys. Fluids* **22**, 052104 (2010).
15. D. Vella, *Langmuir* **24**, 8701–8706 (2008).
16. M. Burrows, *J. Exp. Biol.* **216**, 1973–1981 (2013).
17. Q.-S. Zheng, Y. Yu, X.-Q. Feng, *J. Adhes. Sci. Technol.* **23**, 493–501 (2009).
18. J. B. Keller, *Phys. Fluids* **10**, 3009 (1998).
19. X.-Y. Ji, J.-W. Wang, X.-Q. Feng, *Phys. Rev. E* **85**, 021607 (2012).
20. D. Vella, D.-G. Lee, H.-Y. Kim, *Langmuir* **22**, 5979–5981 (2006).
21. D.-G. Lee, H.-Y. Kim, *J. Fluid Mech.* **624**, 23 (2009).
22. M. Noh, S.-W. Kim, S. An, J.-S. Koh, K.-J. Cho, *IEEE Trans. Robot.* **28**, 1007–1018 (2012).
23. J.-S. Koh, S.-P. Jung, R. J. Wood, K.-J. Cho, A jumping robotic insect based on a torque reversal catapult mechanism. *2013 IEEE/RSJ International Conference of Intelligent Robots and Systems* (2013), pp. 3796–3801.
24. R. J. Wood, S. Avadhanula, R. Sahai, E. Steltz, R. S. Fearing, *J. Mech. Des.* **130**, 052304 (2008).
25. R. J. Wood, *IEEE Trans. Robot.* **24**, 341–347 (2008).
26. J. P. Whitney, P. S. Sreetharan, K. Y. Ma, R. J. Wood, *J. Micromech. Microeng.* **21**, 115021 (2011).
27. P. Birkmeyer, K. Peterson, R. S. Fearing, DASH: A dynamic 16g hexapedal robot. *2008 IEEE/RSJ International Conference of Intelligent Robots and Systems* (2009), pp. 2683–2689.
28. K. Y. Ma, P. Chirarattananon, S. B. Fuller, R. J. Wood, *Science* **340**, 603–607 (2013).
29. Ultratech International Incorporated, www.spillcontainment.com/everdry.
30. J. Zhao, X. Zhang, N. Chen, Q. Pan, *ACS Appl. Mater. Interfaces* **4**, 3706–3711 (2012).
31. X. Q. Feng, X. Gao, Z. Wu, L. Jiang, Q. S. Zheng, *Langmuir* **23**, 4892–4896 (2007).

ACKNOWLEDGMENTS

This work was supported by National Research Foundation of Korea (grant nos. 2013K000371, 2014048162, 2014023206, and 2013R1A2A2A01006394), a grant to Bio-Mimetic Robot Research Center funded by Defense Acquisition Program Administration (grant no. UD130070ID), and the Wyss Institute for Biologically Inspired Engineering. We thank H. Choi and B. Shin for their helpful discussions.

SUPPLEMENTARY MATERIALS

www.sciencemag.org/content/349/6247/517/suppl/DC1
Materials and Methods
Supplementary Text
Figs. S1 to S13
Tables S1 to S7
Movies S1 to S5

20 March 2015; accepted 11 June 2015
10.1126/science.aab1637

PALEOMAGNETISM

A Hadean to Paleoarchean geodynamo recorded by single zircon crystals

John A. Tarduno,[1,2]* Rory D. Cottrell,[1] William J. Davis,[3] Francis Nimmo,[4] Richard K. Bono[1]

Knowing when the geodynamo started is important for understanding the evolution of the core, the atmosphere, and life on Earth. We report full-vector paleointensity measurements of Archean to Hadean zircons bearing magnetic inclusions from the Jack Hills conglomerate (Western Australia) to reconstruct the early geodynamo history. Data from zircons between 3.3 billion and 4.2 billion years old record magnetic fields varying between 1.0 and 0.12 times recent equatorial field strengths. A Hadean geomagnetic field requires a core-mantle heat flow exceeding the adiabatic value and is suggestive of plate tectonics and/or advective magmatic heat transport. The existence of a terrestrial magnetic field before the Late Heavy Bombardment is supported by terrestrial nitrogen isotopic evidence and implies that early atmospheric evolution on both Earth and Mars was regulated by dynamo behavior.

The oldest previously reported geomagnetic field values, from 3.2 billion– to 3.45 billion–year-old magnetite bearing single feldspar and quartz phenocrysts from igneous rocks of the Nondweni and Barberton Greenstone Belts (Kaapvaal Craton, South Africa) (*1*–*3*), indicate a relatively strong field, but the prior history of the geodynamo is unknown. Some thermal evolution models predict no geodynamo before ~3.5 billion years ago (Ga) (*4*).

For magnetic minerals to be suitable recorders, they must be small, in the single to pseudosingle domain state (*5*), and have remained pristine since formation. The metamorphism that has affected Paleoarchean and older rocks makes paleointensity determination especially difficult. These metamorphosed rocks typically contain large multidomain magnetic grains (MD) with short relaxation times, secondary magnetic remanence carriers, and minerals with a propensity

[1]Department of Earth and Environmental Sciences, University of Rochester, Rochester, NY 14627, USA. [2]Department of Physics and Astronomy, University of Rochester, Rochester, NY 14627, USA. [3]Geological Survey of Canada, Ottawa K1A 0E8, Canada. [4]Department of Earth and Planetary Sciences, University of California, Santa Cruz, CA 95064, USA.
*Corresponding author. E-mail: john.tarduno@rochester.edu

Jumping on water: Surface tension–dominated jumping of water striders and robotic insects

Je-Sung Koh *et al.*

Science **349**, 517 (2015);
DOI: 10.1126/science.aab1637

www.sciencemag.org/content/349/6247/517/suppl/DC1

Supplementary Material for

Jumping on water: Surface tension–dominated jumping of water striders and robotic insects

Je-Sung Koh, Eunjin Yang, Gwang-Pil Jung, Sun-Pill Jung, Jae Hak Son, Sang-Im Lee, Piotr G. Jablonski, Robert J. Wood, Ho-Young Kim,* Kyu-Jin Cho*

*Corresponding author. E-mail: hyk@snu.ac.kr (H.-Y.K.); kjcho@snu.ac.kr (K.-J.C.)

Published 31 July 2015, *Science* **349**, 517 (2015)
DOI: 10.1126/science.aab1637

This PDF file includes:

Other Supplementary Material for this manuscript includes the following:
(available at www.sciencemag.org/content/349/6247/517/suppl/DC1)

Materials and Methods

1. Measurements of and Experiments on Water Striders Jumping Water

Water striders (*Aquarius paludum*) were collected from streams and ponds around the city of Seoul, Korea. Insects were placed individually in a square acrylic bath (70 mm wide) half-filled with water (normal tap water), and their jumping behaviors were recorded from front and side views simultaneously, using two high-speed cameras (TS 1000ME) at 1000 frames per second. Four jumps by four adult water striders were recorded and analyzed. The inclinations of the jump trajectory were between 60° and 80° of the horizontal (two jumps by two males and two jumps by two females; see Table S1 for kinematic parameters). The jumps were induced by touching the insect with a rigid stick positioned below its body; all the analyzed jumps were checked to verify that the jumping motion was not influenced by the stimulating stick. Because we only focused on vertical jumping speed from the water surface, we measured only the vertical component of motion of the insects' legs and bodies from the movies. The animals used in this study were handled in accordance with institutional guidelines for the care and use of laboratory animals.

2. Measurements of and Experiments on the Robot

Velocity and position data were captured by vision analysis software (Proanalyst). The jumping video was recorded by a high-speed camera system (MotionXtraNx3-S3, IDT Ltd., UK) at 3000 frames per second. Seven tracking points were put on the robot structure, and the velocity and position of the virtual center of mass were computed from data collected from these points. Finally, velocity and position were plotted to a millisecond resolution (Figs. S1-S3).

The robot was untethered but triggered by external heat. The heating wire (Ni-Cr wire) protruded 1 mm from the free surface, and the actuator was positioned right above the heating wire when the robot was put on the free surface. The actuator was heated by thermal convection around the heating wire until the torque direction reversed.

3. Fabrication and Materials

The robot structure was designed so that the smart composite microstructures (SCM) manufacturing process could be applied (*24*). This process facilitates the development of microscale linkage structures by lamination of multiple sheets cut by precision laser machining. In this manufacturing process, the planar folding pattern creates 3D shapes that become the final robot structure after adhesion. The structure is primarily composed of glass fiber reinforced plate (GFRP), which is made by curing five layers of fabric glass prepreg (Realcarbon Co.) in a heat press (140°C, 550 kPa, 1 hr). The GFRP was cut by a UV laser machining system (AWAVE- 355nm-3W-Nd:YVO4-DPSS laser, Advanced Optowave Co.) (Fig. S5).

Supplementary Text

1. Stiffness of the Sheet SMA Actuator

The stiffness of the shape memory alloy (SMA) actuator, k, is increased by increasing the temperature of the actuator. It is difficult to measure and control the

temperature precisely. Reliable actuator stiffness may be calculated by modeling the passive trigger component and the stroke of the actuator. The beam deflection model is employed to obtain the triggering force, and the stroke of the sheet SMA coil actuator can be measured. The force and deflection of the passive trigger is expressed in equation (1), the cantilever deflection model with the width and thickness of the passive trigger as illustrated in Fig. S6 A and B,

$$F \cdot \alpha = 2 \cdot \frac{2EI}{L_t^{\,2}} \delta \quad (I = \frac{w\tau^3}{12}) \tag{1}$$

where F is the actuation force, α is the moment arm of the passive trigger, L_t is the length, w is the width of the cantilever, τ is the cantilever thickness, δ is the required deflection for passive triggering, and E is the characteristic modulus of the composite material.

The characteristic modulus of the composite material should be obtained by experiments on specimens with passive triggers of varying widths and thicknesses, to produce varying degrees of stiffness. Experiments were performed on a range of passive trigger specimens to determine the relationship between pulling force and deflection (Fig. S6C). The characteristic modulus of the composite materials was computed to be 0.93 Gpa, and the modeling results with this values matched well with experiments (Fig. S6D). Using the model, we can design the triggering force of the passive trigger when it attains the required deflection for triggering. The required deflection is determined by the initial body angle, θ. The prototypes have the same initial angle of 32°, which corresponds to 0.8 mm of desired deflection. Finally, the stiffness of the actuator, k, can be calculated by dividing the triggering force by actuator stroke:

$$Actuator\ Stiffness\,(k) = \frac{Triggering\ Force\,(F)}{Actuator\ Stroke\,(s)} \tag{2}$$

By varying the design of the passive trigger, various robot prototypes with different actuator stiffnesses were prepared. Table S2 lists their driving forces.

2. Water Surface Modeling for the Real and the Robotic Water Strider

The lifting force in jumping on water is created from various hydrodynamic forces that are in effect between the driving legs and the water surface. During jumping on the ground the reaction force on a rigid surface directly lifts the body. Fig. S7 shows the dynamic parameters for the real and the robotic water strider and the hydrodynamic forces between the leg and the water surface. The drag force due to form drag and skin friction, F_d, is exerted on the moving leg with a certain velocity. The buoyancy, F_b, and the surface tension force, F_s, correspond to the weight of water that would fill the dimple. The added inertia, F_i, arises when the fluid is accelerated by the accelerating leg. Then we may write the total forces as follows (*14*):

$$F_w \approx \underbrace{C_d \rho r L_s U^2}_{F_d} + \underbrace{\left(\frac{\pi}{2}\rho g r^2 L_s + 2\rho g r d L_s\right)}_{F_b} + \underbrace{\pi \rho r^2 L_s a}_{F_i} + \underbrace{2\sigma L_s}_{F_s} \tag{3}$$

Drag Buoyancy Added mass Surface tension

where C_d is the drag coefficient, ρ is the density of water, U is the speed of the leg, L_s is the wetted length of the leg, g is the gravitational acceleration, h is the depth of the

dimple, a is the acceleration of the leg, σ is the surface tension coefficient, and r is the radius of the leg.

On the water surface, driving force is generated by hydrodynamic forces exerted on the driving legs when the legs push down the water surface. The force ratios for water striders and robotic striders with regard to the surface tension force are scaled as $F_d/F_s \sim 10^{-2}$, $F_b/F_s \sim 10^{-2}$, and $F_i/F_s \sim 10^{-3}$. The hydrodynamic forces differ depending on whether the legs break the water surface or not, because the surface tension force—the largest of the hydrodynamic forces—is lost when the surface is broken. Using characteristic values for water strider locomotion, the approximate magnitudes of each term in the hydrodynamic equation (3) were estimated. The characteristic parameters of water strider locomotion listed in Table. S4, have been adopted from Vella *et al. (14)*.

Table S5 shows the calculated dimensionless numbers to compare the scales of various hydrodynamic forces. Comparing the water strider and the robot, the values are similar, and we can deduce the force exerted by the surface tension of the water is much larger than the other forces. The thin, wire-shaped legs have very small characteristic area and volume, which minimizes form drag, buoyancy, and the added mass effect. The viscous force is small with the velocity of common arthropods on water. Therefore, the surface tension force is the dominant factor in the reaction force of the water jumping arthropods. However, this is true only if the water surface is unbroken. If the legs penetrate the water surface, the surface tension force disappears immediately.

A sudden drop in the supporting force on water drastically decreases the takeoff velocity. In terms of the energy transfer, the momentum of water around the legs increases when the legs break the water surface, and the energy loss to the kinetic energy of water reduces the vertical kinetic energy of the water strider. E_s (the stored energy in the actuator) is transferred into the kinetic energy of the robot ($1/2\ mv_b^2$), water kinetic and surface energy, vibration, friction, and so forth.

$$E_s \rightarrow \frac{1}{2} m v_b^{\,2} + water\ kinetic\ E + water\ surface\ E + vibration + friction\ \ loss + \ldots \tag{4}$$

When the water kinetic and surface energy are increased in a constant stored energy, the kinetic energy of the jumping body is reduced.

The surface tension force is the dominant force for locomotion on water (*2, 4, 6, 11, 27, 28*). In this study, the static calculation is used to estimate the capillary force on the moving leg following a calculation of the Weber number. Vella (*14*) reported the sinking characteristics of the cylinder impinging on the liquid surface. That study describes the effect of *We* on sinking dynamics, showing that the maximum deformation of meniscus upon sinking with small *We* converges to that of a cylinder gently placed on the liquid surface. In addition, the load bearing capacity of a liquid surface with a small Froude number ($F=U/(gl_c)^{1/2}$) does not differ much from the static load bearing capacity.

Vella's study addressed small objects that impinge with initial velocity and are subsequently decelerated by the liquid. In contrast, the legs of real water striders, and of our robot, initially rest on the surface, leading to much smaller acceleration of water in the early stage than in the impinging cylinder case. Although these two motion are not the same, the qualitative tendency toward negligible dynamic effects with small *We* would still be valid for the leg stroke during water jumping. Since the *We* of the water striders and our robot, as listed in Table S5, are small enough to assume a surface-tension-

dominant phenomenon with negligible dynamic effects, the interfacial force estimation based on the depth of the meniscus can be applied. As a result, the model yields simulations that are well-matched with our experiments within 7% error in take-off velocity.

We measured the surface tension force around the leg of the robot prototype experimentally. We prepared two leg shapes (round and square) and used a tensile test machine with a precise electronic balance to push the specimens down on the water surface, as shown in Fig. S8. The experiments were performed with raw wire and hydrophobic coated wire in two shapes to determine the effect of hydrophobicity. With the hydrophobic coating, 150° of the contact angle is achieved, whereas the raw SMA wire achieves only 75°, as shown in Fig. S9. Results obtained for the round-shaped leg show a linear relationship between the surface tension force and depth (Fig. S10). The shape of the leg influences the surface tension force because it affects the depth of the wetted legs. Actually, water striders have flexible legs that are held bent when they float and move on water. The surface tension force around a cylinder bent on the water surface has been studied, and it can be computed analytically (*14, 29*). Based on this research, we can compute the surface tension force around the leg of the robotic water strider.

The surface tension force per unit length, f_c, is shown in the following equation:

$$f_s(h) = 2\rho g l_c \cdot h\sqrt{1-\left(h/2l_c\right)^2} \tag{5}$$

$$l_c = \sqrt{\frac{\sigma}{\rho g}}$$

where ρ is the density of water, g is the gravitational acceleration, h is the depth of the center of the cylinder beneath the free surface of water, and l_c is the capillary length of water. The resulting surface tension force of the leg (F_s) is the integration of the surface tension force per unit length along the wetted length (L_s). This is shown in Fig. S11.

$$F_s(h) = \int f_s(h)\, dL_s \tag{6}$$

The modeling results and experimental measurements match well, as shown in Fig. S12. For the round-shaped leg, error increases as depth increases. The measured force becomes smaller than the modeling force because the actual contact length is reduced by deformation of the free surface, as shown in Fig. S11. The round-shaped leg shows a more linear relationship between surface tension force and depth, like a linear spring. Therefore, the slope of the graph is assumed to be the stiffness of the water surface. By modeling the water surface as a spring-damper system, dynamic modeling of the robot for jumping on water is simplified and easily simulated. Table S6 lists the stiffness values of the water surface measured in experiments.

3. Dynamic Modeling of the Robot

The surface tension force is modeled as a spring-damper system due to the force linearly increasing with the depth of dimple as long as the water surface is not broken (Fig. S10). Therefore, a Lagrange formulation for the differential equations of motion can be derived with the following energy equation:

$$\frac{d}{dt}\left(\frac{\partial L}{\partial \dot{\theta}}\right)-\frac{\partial L}{\partial \theta}=-C_w(\dot{\theta}) \tag{7}$$

where $L = T - V$,

$$T=\sum\frac{1}{2}m_i v_i^2+\sum\frac{1}{2}I_i w_i^2$$

$$V=\frac{1}{2}ks^2+\sum\frac{1}{2}m_i gH_i+\frac{1}{2}k_w h^2$$

where T is the kinetic energy, V is the potential energy, v_i is the velocity of each component, C_w is the damping coefficient, I_i is the second moment of inertia, w_i is the angular velocity of each component, g is the gravitational acceleration, and H_i is the height from the ground level. k_w is the stiffness of the water surface, and h is the sinking depth of the legs. k_w varies depending on the length and shape of the wetted part of the legs. In the previous section, we obtained the stiffness of the water surface with the specimen that has the same leg dimensions (Fig. S13). Therefore, we use 0.375 N/m for k_w, the stiffness of the water surface in the dynamic modeling. The damping coefficient (C_w), 0.01, has been obtained from slope of first derivative of the drag force with respect to the sinking velocity.

4. Results and Data

Table S2 lists values from our experimental results and dynamic modeling. The driving force profile is obtained from dynamic modeling owing to practical difficulties in measuring small forces exerted for short durations (Fig. S4). Dynamic modeling produces velocity profiles that match well to the experimentally obtained profiles of jumping on ground, as shown in Fig. S3. However, experimental results on water (except for Fig. S3D) do not match well with the results obtained from the dynamic model because the water surface was broken, which changed the driving force significantly. Wetted length was measured using a video analysis program at the moment of maximum dimple depth. Maximum driving force per wetted length of robot 4 is just below the maximum surface tension force (2σ), 144 mN/m. Therefore, robot 4 shows similar jumping performance on both water and ground (Fig. S3D).

The initial energy stored in the actuator is transformed into the jumping kinetic energy which is then transformed into the gravitational potential energy as the jumping height increases. However, some portion of the energy is dissipated into the vibration kinetic energy of the legs and the robot body, as well as the water surface energy when jumping on water.

The amount of energy transformation is calculated using our dynamic model at the moment of take-off for robot 4, which satisfies the design criteria, and is listed in Table. S7. When jumping on ground, the kinetic energy stored in the vibrations of the legs and the body is 67.4%, and the kinetic energy for jumping is 29.3%. Note that the body has already gained potential energy of 3.3% at take-off. When jumping on water, the kinetic

energy stored in the vibration is 63.5% and energy stored in the water surface is 2%, and the kinetic energy for jumping is 31.3% with potential energy of 3.3%. Note that less energy is dissipated to vibration energy when jumping on water.

Although the energy lost to friction is not included in our models, the amount of energy lost to friction can be estimated from the discrepancy between the modeling and the experimental results of the take-off velocity on ground (see Table S2). The maximum discrepancy occurred for robot 4, showing less than 3% of the initial stored energy.

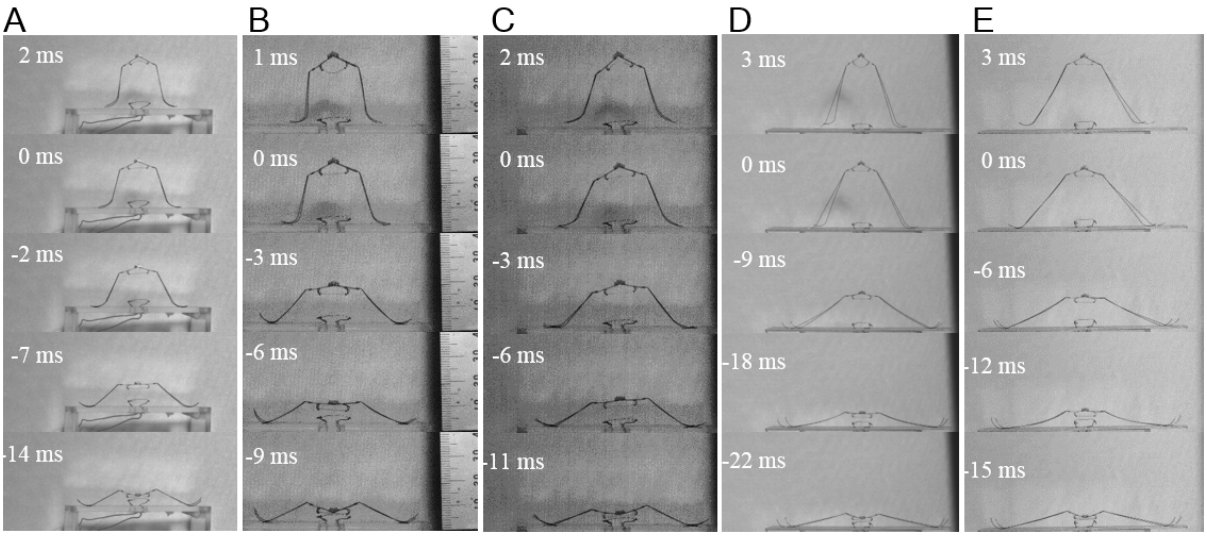

Fig. S1.

Sequential pictures taken by a high-speed camera during take-off on the ground. (A) Robot 1. (B) Robot 2. (C) Robot 3. (D) Robot 4. (E) Robot 5.

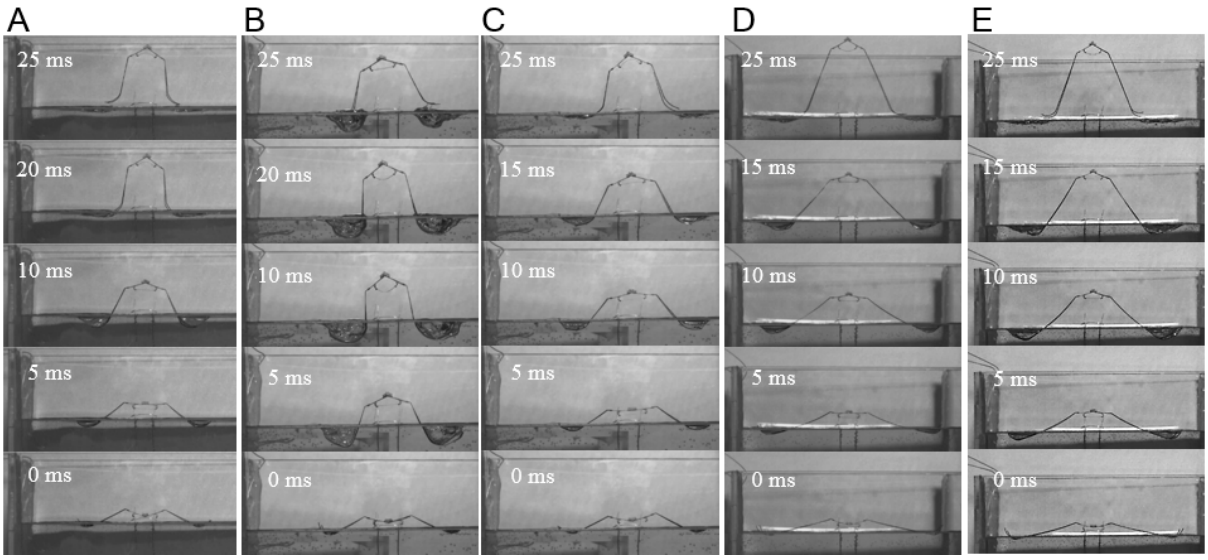

Fig. S2

Sequential pictures taken by a high-speed camera during takeoff on water. (A) Robot 1. (B) Robot 2. (C) Robot 3. (D) Robot 4. (E) Robot 5.

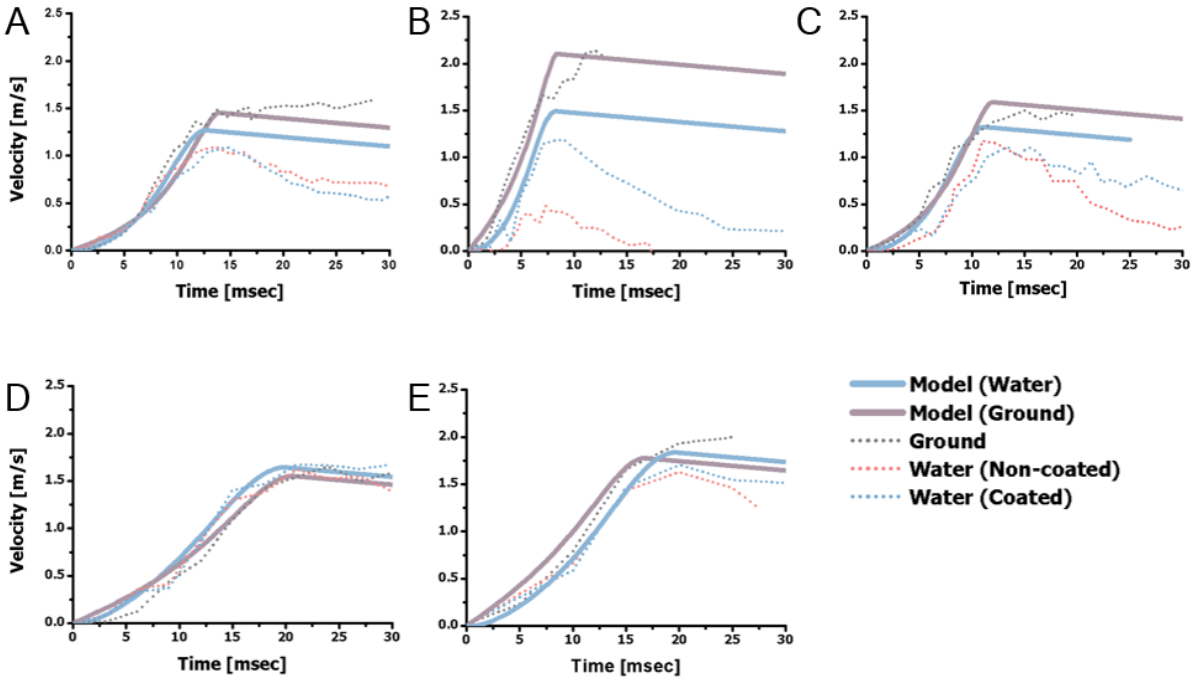

Fig. S3

Velocity of the robot during take-off. The graphs were obtained from experiments and dynamic modeling. (A) Robot 1. (B) Robot 2. (C) Robot 3. (D) Robot 4. (E) Robot 5.

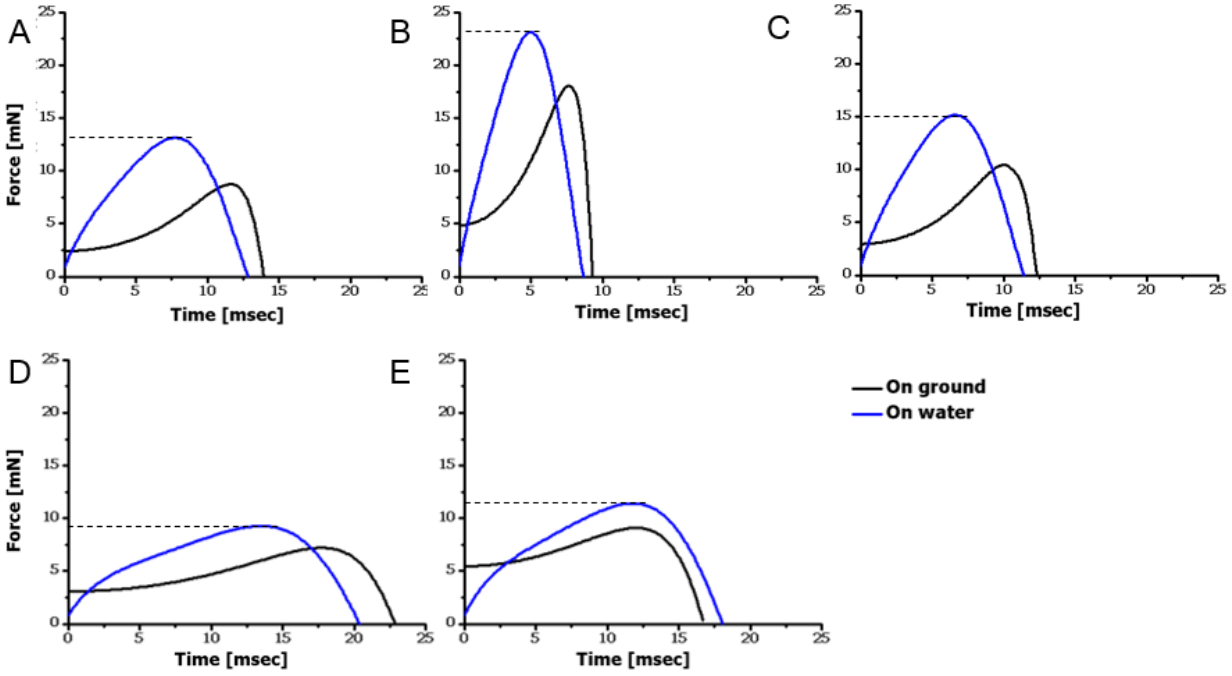

Fig. S4

Driving force profiles obtained by dynamic modeling. (A) Robot 1. (B) Robot 2. (C) Robot 3. (D) Robot 4. (E) Robot 5.

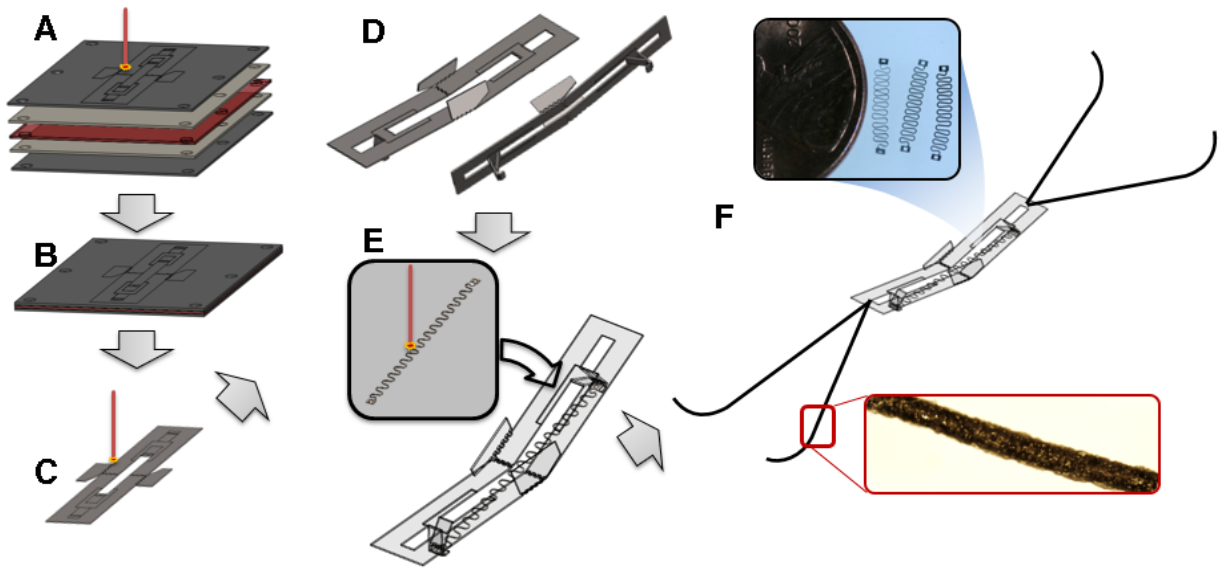

Fig. S5

Fabrication of the jumping robotic insect using SCM (*18, 20, 22*). (A) Ultraviolet (UV) laser machining of each layer (fiber-reinforced polymers [FRP]-adhesives-polyimide film-adhesives-FRP). (B) Laminating with a heat press. (C) Final cut by UV laser machining to release the functional components. (D) Assembly by folding and locking. (E) Attaching the sheet SMA actuator using SMP blind riveting (*29*). (F) Attaching legs made of superelastic SMA wire coated with superhydrophobic materials.

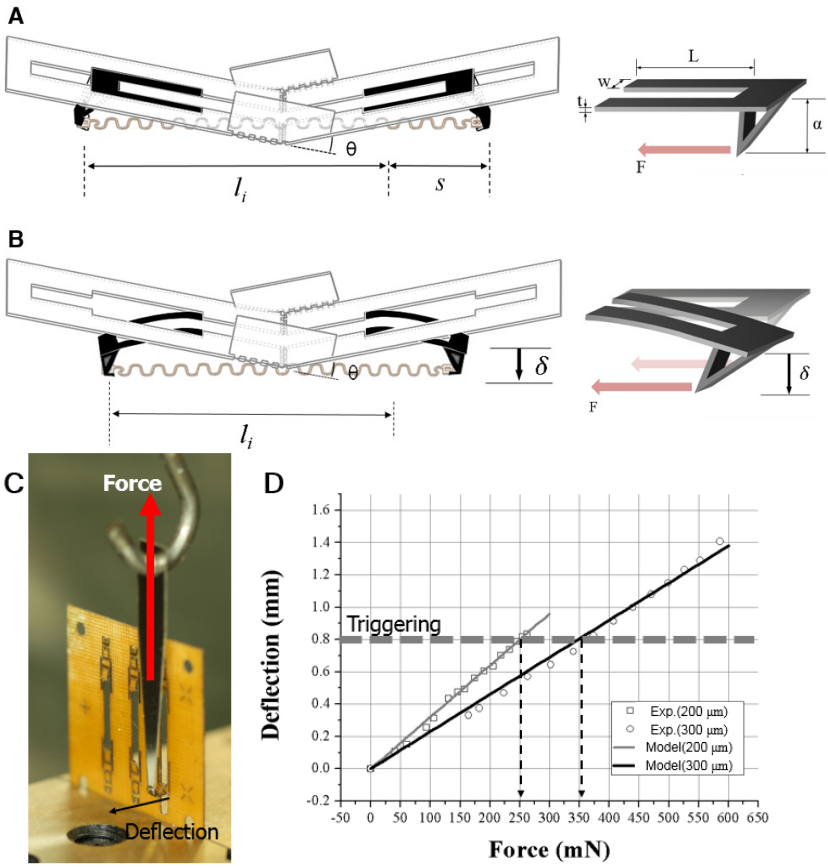

Fig. S6

Illustration of the passive trigger component parameters. (A) Before actuation. (B) The moment of triggering. (C) Experimental setup. (D) Experimental data and modeling results with various widths (w).

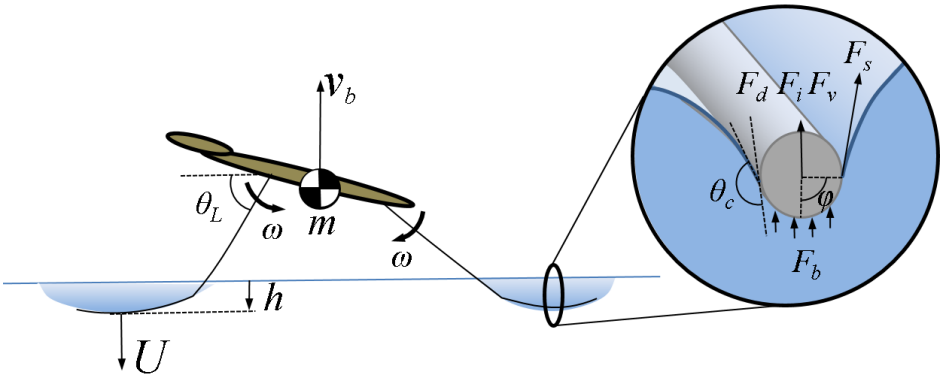

Fig. S7

Illustration of the hydrodynamic forces exerted on the leg of the water strider and robotic water strider at the water surface.

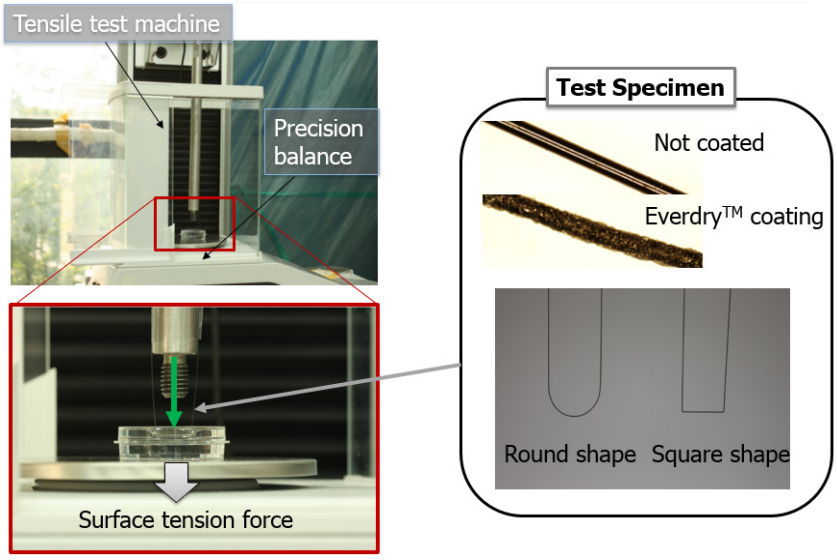

Fig. S8
Experimental setup for measuring the surface tension force at the leg tip.

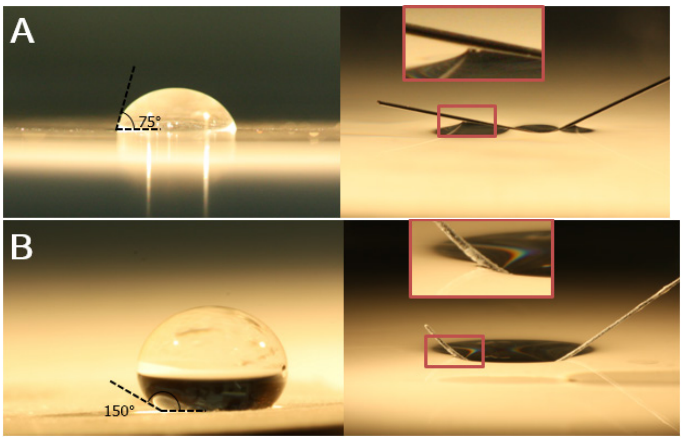

Fig. S9

(A) Uncoated SMA (left: Nitinol sheet, right: Nitinol wire). (B) SMA (Nitinol) coated with hydrophobic material (EverDryTM, UltraTech International Inc., left: Nitinol sheet, right: Nitinol wire).

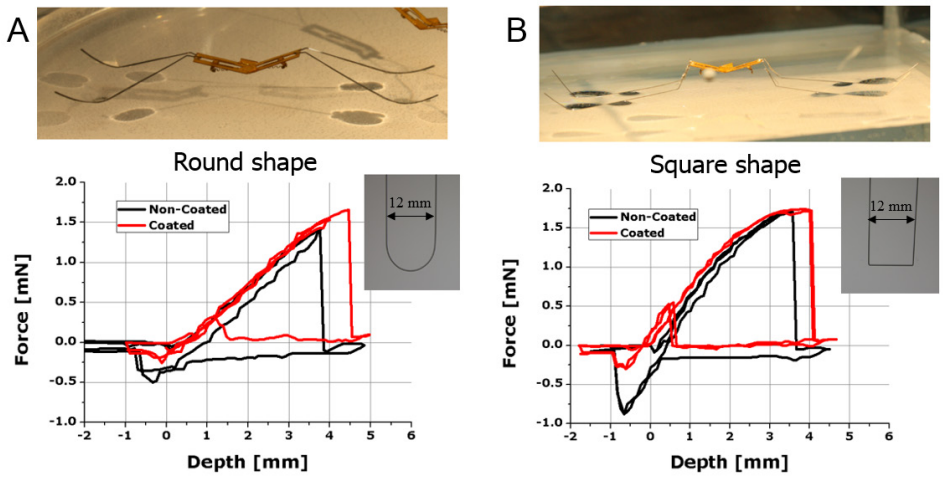

Fig. S10

Measurement results of measuring the stiffness of the water surface. (A) Round shape leg. (B) Square shape leg.

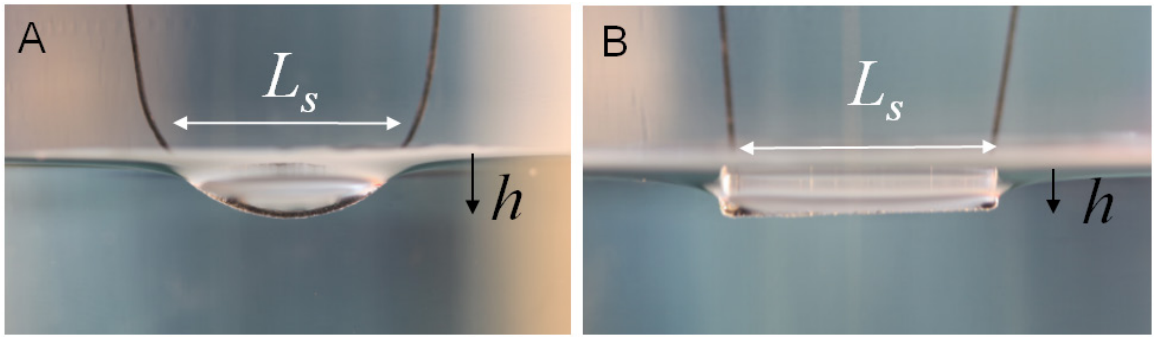

Fig. S11

Side view of experimental measurement of the surface tension force. (A) Round-shaped leg. (B) Square-shaped leg.

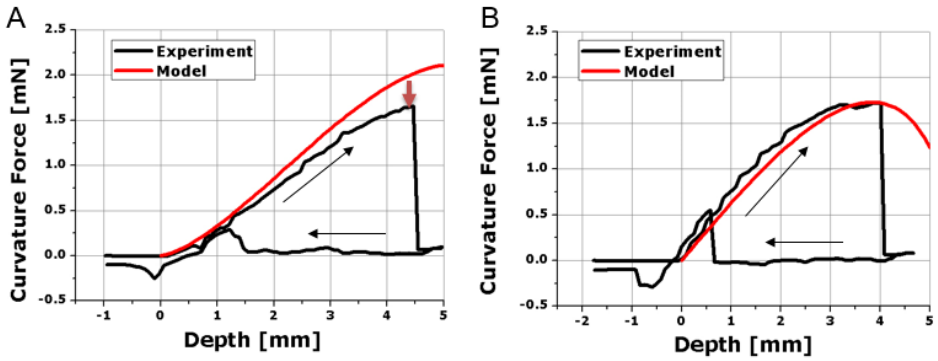

Fig. S12

Analytical modeling and experimental measurement of the surface tension force of the round-shaped leg (A) and the square-shaped leg (B).

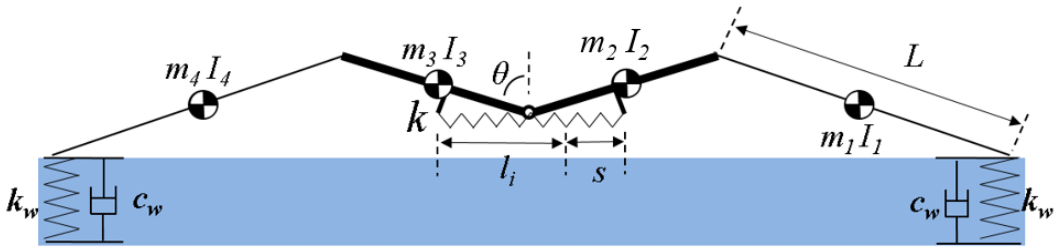

Fig. S13
Dynamic model of the robotic water strider jumping on water.

	Water strider 1	Water strider 2	Water strider 3	Water strider 4
Symbol in Fig. 2	□	■	○	●
Sex	Male	Male	Female	Female
Body mass [mg]	38.4	37.2	49.0	49.0
Wetted length [mm]	46.4	43.6	44.6	44.6
Maximum dimple depth [mm]	2.49	2.88	2.97	2.98
Maximum force [mN]	5.61	5.83	6.07	6.08
Maximum force per unit length [mN/m]	121	133	136	136
Velocity at maximum depth [m/s]	0.92	0.95	0.89	0.69
Take-off velocity [m/s]	1.17	1.30	1.22	0.98
Take-off velocity / Velocity at maximum depth	1.27	1.37	1.37	1.42
Water surface	Not broken	Not broken	Not broken	Not broken

Table S1.
Kinematic parameters of water strider subjects

	Robot 1	Robot 2	Robot 3	Robot 4	Robot 5
Max. driving force on the ground (modeling) [mN]	8.74	18	10.49	7.2	9.09
Max. driving force on water (modeling) [mN]	13.13	23.12	15.15	9.27	11.42
Wetted length [mm]	48	48	48	66	66
Max. driving force (f) / wetted length (l) [mN/m]	273	481	315	140	173
Take-off velocity on the ground (experiment) [m/s]	1.45	2.1	1.48	1.53	2
Take-off velocity on the ground (modeling) [m/s]	1.45	2.11	1.6	1.62	1.9
Take-off velocity on water (experiment) [m/s]	0.6	0.25	0.6	1.67	1.4
Take-off velocity on water (modeling) [m/s]	1.26	1.5	1.4	1.67	1.9
Water-ground velocity ratio (ε_w)	0.41	0.11	0.4	1.09	0.7
Jumping height on ground (experiment) [mm]	107	225	111	119	204
Jumping height on ground (modeling) [mm	107	227	131	134	184
Jumping height on water (experiment) [mm]	18	3	18	142	100
Jumping height on water (modeling) [mm]	81	114	100	142	184
Water surface	Broken	Broken	Broken	Not broken	Broken

Table S2.

Experimental and dynamic modeling results

	Robot 1	Robot 2	Robot 3	Robot 4	Robot 5
Body mass [mg]	53	64	53	68	68
Leg length [cm]	3			5	
Leg width [mm]	0.2				
Triggering force [mN]	95	201	118	95	118
Actuator stroke [mm]	5.75		4.5	5.75	
Actuator stiffness [N/m]	16.52	35	26	16.52	20.5
Initial angle of the body [°]	32				
Width of passive trigger cantilever [µm]	200		250	200	250
Composite thickness [µm]	170	240	170		

Table S3.

Specifications of the robotic water strider prototypes

Parameter	Description	Characteristic value
C_d	Drag coefficient of the leg	2 at Re~10-10^2
ρ	Density of water	10^3 kg/m^3
σ	Coefficient of surface tension of water	0.072 N/m
v	Coefficient of kinematic viscosity of water	10^{-6} m^2/s
g	Gravitational acceleration	9.8 m/s^2
U	Mean velocity of the leg	0.16 m/s (real) 0.24 m/s (robot)
l	Wetted length of leg	10 mm (real) 20 mm (robot)
P	Leg contact perimeter of four legs	80 mm (real) 160 mm (robot)
R	Radius of leg	0.05 mm (real) 0.1 mm (robot)
D	Diameter of leg	0.1 mm (real) 0.2 mm (robot)
M	Mass	40 mg (real) 68 mg (robot)

Table S4.

Characteristic parameters for biological and robotic water strider locomotion

Parameter	Water strider	Robot
$Re = UD/\nu$	16	48
$Bo = \rho g R^2/\sigma$	3×10^{-4}	1×10^{-3}
$We = \rho U^2 D/\sigma$	0.036	0.165
$Ba = Mg/\sigma P$	0.07	0.06

Table S5.
Dimensionless parameters for real and robotic water strider locomotion

Parameters		Round shape	Square shape
Stiffness of the water surface	Not coated	0.375 N/m	Nonlinear
	Coated	0.375 N/m	Nonlinear
Maximum surface tension force	Not coated	0.057 N/m	0.08 N/m
	Coated	0.07 N/m	0.08 N/m

Table S6.
Stiffness of the water surface obtained from the surface tension force measurement

Energy	On ground	On water
Initial energy in the actuator	0.304 mJ (100%)	0.304 mJ (100%)
Jumping kinetic energy	0.089 mJ (29.3 %)	0.095 mJ (31.3 %)
Vibration kinetic energy	0.205 mJ (67.4 %)	0.193 mJ (63.5 %)
Potential energy	0.010 mJ (3.3 %)	0.010 mJ (3.3 %)
Water surface energy	0.000 mJ (0 %)	0.006 mJ (2.0 %)

Table S7.

Transformation of the initial energy to various energies at the moment of take-off for robot 4 (in modeling)

Movie S1

Movie clip of the robotic insect performing a smooth jump on the water surface without making a large splash. The movie plays at 0.005X real-time speed and was taken with a from high-speed camera recording at 3000 frames per second. The robot is prototype number 4, which satisfies the design criteria described in the paper.

Movie S2

Movie clip of a horizontal view of movie S1. The movie plays at 0.005X real-time speed and was taken with a high-speed camera recording at 3000 frames per second. Distortion of the water surface is shown, and the water surface supports the driving force of the legs successfully without breaking.

Movie S3

Movie clip of the robotic insect jumping on the rigid ground. The movie plays at 0.005X real-time speed and was taken with a high-speed camera recording at 3000 frames per second.

Movie S4

Movie clip showing robot prototype 4 jumping on water and on ground. The jumping heights in the two experiments are almost similar. The movie shows that the robot obtains almost the same momentum on water as on rigid ground. The movie plays at 1/8X real-time speed and was taken with a high-speed camera at 240 frames per second.

Movie S5

Movie clip showing water strider jumping on water in front view. The movie plays at 0.03X real-time speed. The water strider was placed in a square acrylic bath (70 mm wide) half-filled with water, and jumping behaviors were recorded from front view using a high-speed camera (TS 1000ME) at 1000 frames per second.